Journal of Energy Chemistry 110 (2025) 768–777

Contents lists available at ScienceDirect

Journal of Energy Chemistry

journal homepage: www.elsevier.com/locate/jechem

http://www.journals.elsevier.com/journal-of-energy-chemistry/

Copper nanoclusters featuring fully inorganic anionic ligands for enhanced electrocatalytic nitrate-to-ammonia conversion

Xi Chen [a], Fasheng Chen [a], Xin-yu Zhong [d], Junjie Ding [e], Huaizhu Wang [b], Liwen Dai [a], Xinchuan Ma [a], Hui Wang [a], Chang Wu [a], Xiao Li [c,*], Yan Xiong [b,*], Zhong Jin [b,*], Minghang Jiang [a,b,*]

[a] Department of Chemistry, School of Science, Xihua University, Chengdu 610039, Sichuan, China
[b] State Key Laboratory of Coordination Chemistry, MOE Key Laboratory of Mesoscopic Chemistry, MOE Key Laboratory of High Performance Polymer Materials and Technology, MOE Engineering Research Center of Photoresist Materials, Jiangsu Key Laboratory of Advanced Organic Materials, Tianchang New Materials and Energy Technology Research Center, Institute of Green Chemistry and Engineering, School of Sustainable Energy and Resources, School of Chemistry and Chemical Engineering, Nanjing University, Nanjing 210023, Jiangsu, China
[c] College of Chemistry and Food Science, Yulin Normal University, Yulin 537000, Guangxi, China
[d] Shanghai Institute of Applied Physics, Chinese Academy of Sciences, Shanghai 201800, China
[e] College of Physics and Center of Quantum Materials and Devices, Chongqing University, Chongqing 401331, China

ARTICLE INFO

Article history:
Received 7 May 2025
Revised 4 July 2025
Accepted 4 July 2025
Available online 18 July 2025

Keywords:
Amorphous Cu(OH)Cl nanoclusters
Low-coordination Cu atoms
Crystalline modulation engineering
Nitrate electroreduction reaction
Ammonia electrosynthesis

ABSTRACT

Atomically precise copper-based nanoclusters stand out as one of the highly promising catalysts in the realm of electrochemical nitrate reduction reaction (NITRR) aimed at ammonia (NH_3) synthesis. However, the controllable synthesis of stable Cu-based nanoclusters featuring fully inorganic anionic ligands for electrochemical NITRR remains a challenge. Herein, we present a simple and gentle chelated co-precipitation method for the uniform growth of ultrafine amorphous Cu(OH)Cl (a-Cu(OH)Cl) nanoclusters, featuring a diameter of approximately 9 nm, onto carbon nanotubes (a-Cu(OH)Cl/CNTs), aimed at enhancing electrocatalytic NITRR performance. Intriguingly, trisodium citrate dihydrate (TCD) could effectively change the crystalline form of Cu-based nanoclusters to obtain a-Cu(OH)Cl nanoclusters instead of high-crystallinity $Cu_2(OH)_3Cl$ (c-$Cu_2(OH)_3Cl$) nanoclusters. In comparison to c-$Cu_2(OH)_3Cl$ nanoclusters, a-Cu(OH)Cl nanoclusters, featuring a smaller particle size and containing more low-coordination Cu atoms, provide more efficient catalytic sites, thereby enhancing the reaction rate and energy efficiency for NH_3 production. The proposed chelated co-precipitation method provides a promising crystalline modulation engineering strategy to boost the electrocatalytic performances of metal nanoclusters.

1. Introduction

NH_3 plays a pivotal role as a foundational chemical in both modern industry and agriculture [1–5]. Furthermore, it functions as a carbon–neutral and environmentally friendly fuel, primarily manufactured through the Haber-Bosch process under high-temperature conditions ranging from 650 to 750 K and high-pressure conditions ranging from 200 to 350 atm (1 atm = 105 Pa) [6,7]. However, this technology consumes approximately 1 %–2 % of the world's annual energy supply and accounts for roughly 1 % of total global energy-related CO_2 emissions [8–10]. To address the escalating global energy demands and pressing environmental pollution concerns, it is advisable to develop more environmentally and friendly methods for artificial ammonia synthesis [11,12]. The yearly combustion of fossil fuels worldwide, extensive utilization of nitrogen-based fertilizers, significant release of industrial wastewater (with nitrate concentrations typically at 2000 ppm), and the widespread presence of niter ore (primarily in Chile and China's Turpan Basin) contribute to the abundant presence of nitrate sources in the natural environment [13–16]. Additionally, the excessive accumulation of nitrate in drinking water can lead to human health issues [17]. Hence, the electrochemical conversion of nitrate into ammonia offers a highly promising approach for nitrogen recycling and mitigating environmental pollution issues.

* Corresponding authors.
E-mail addresses: leex211@126.com (X. Li), xiongyan@nju.edu.cn (Y. Xiong), zhongjin@nju.edu.cn (Z. Jin), minghang@mail.xhu.edu.cn (M. Jiang).

https://doi.org/10.1016/j.jechem.2025.07.017

The electrochemical NITRR to NH_3 entails an eight-electron transfer process, which exhibits sluggish kinetics process [18]. Furthermore, the competitive hydrogen evolution reaction (HER) and various byproducts complicate the reaction pathways, rendering the NITRR less selective and efficient [19,20]. Consequently, the design and development of highly efficient electrocatalysts that exhibit high activity and selectivity for electrochemical NH_3 synthesis continues to pose a significant challenge [21]. Over the past of years, an increasing number of studies have been conducted to improve the catalytic performance of the electrochemical NITRR to NH_3 using a Ti- [22], Fe- [23,24], Co– [25,26], Ni- [27–29], Cu- [9,11,18,30–38], Ru- [8,39,40], or Pd-based [41,42] catalysts. Among the various types of NITRR metal-based electrocatalysts, Cu-based materials have been explored as ideal candidates due to their excellent conductivity, capacity to alleviate HER, and distinctive outer electron configuration [18,43]. These attributes endow them with exceptional adsorption capabilities towards NO_3^-. However, due to the limited catalytic sites of pure Cu metal, it poses a challenge to simultaneously enhance the adsorption of diverse reactive species during the electrochemical reduction of NO_3^- [26]. Consequently, there is a necessity to devise Cu-based electrocatalysts featuring abundant catalytic active sites to overcome this limitation. Currently, metal nanoclusters have captured the interest of researchers owing to their adjustable atomic composition and spatial arrangements, coupled with their exceedingly small particle sizes [44,45]. This special structure and nanoscale dimension provides abundant of active sites during the electrocatalytic NITRR, making them promising candidates for enhancing catalytic efficiency and selectivity [40,45]. Currently, Cu nanoclusters predominantly employ organic molecules, including thiolate, alkynyl, N-heterocyclic carbene, and others, as ligands [44–46]. However, in comparison to the predominantly expensive and toxic organic ligands, the employment of inorganic anions (such as OH^- and Cl^-) as ligands holds promise for reducing both the synthesis cost and the environmental footprint during synthesis of Cu nanoclusters. Furthermore, inorganic anions offer the potential to synthesize Cu nanoclusters with extremely small particle sizes, an advantage over organic molecules [47]. Meanwhile, inorganic anions usually bind to metals through highly polar bonds (such as M–Cl) which greatly improve the cluster stability [48], thereby advantageously alleviating issues such as decomposition at reduction conditions. In addition, previous works reported that amorphous metal-based materials possess superior catalytic capability for electrocatalytic NH_3 synthesis compared to their crystalline analogs [8,39,40,49]. This advantage arises from the abundance of low-coordinate atoms present on amorphous metal-based electrocatalysts, which consequently increases the number of catalytic sites, thereby boosting their performance [25,39,50]. Based on the aforementioned analysis, the design and development of amorphous Cu nanoclusters utilizing inorganic anions as ligands are anticipated to function as highly efficient electrocatalysts for electrochemical NITRR to NH_3. However, the controllable preparation of such an amorphous Cu-based nanocluster utilizing inorganic anions as ligands (such as OH^- and Cl^-) via a simple and mild method still remains to be explored.

Herein, we demonstrate the uniform and in situ growth of ultrafine amorphous Cu(OH)Cl nanoclusters, enriched with low-coordination Cu atoms and possessing a diameter of approximately 9 nm, onto CNTs through a facile and gentle chelated co-precipitation method. Notably, the addition of TCD plays a critical role in facilitating the formation of these a-Cu(OH)Cl nanoclusters, which are characterized by a significantly smaller particle size, rather than the generation of larger c-$Cu_2(OH)_3Cl$ nanoclusters. Benefitting from the abundant surface low-coordination Cu atoms and the smaller particle size, the a-Cu(OH)Cl nanoclusters can expose more catalytic active sites during the electrocatalytic NITRR process compared to c-$Cu_2(OH)_3Cl$ nanoclusters. The resulting a-Cu(OH)Cl/CNTs catalyst showed an NH_3 yield of 342.69 μg h^{-1} $mg_{cat.}^{-1}$ and an Faraday efficiency (FE) for NH_3 of 80.2 % at –0.9 V vs RHE, which was significantly higher than that of c-$Cu_2(OH)_3Cl$/CNTs (163.88 μg h^{-1} $mg_{cat.}^{-1}$ and 62.1 %, respectively). The a-Cu(OH)Cl/CNTs catalyst exhibited remarkable stability, maintaining virtually unaltered catalytic activity after consecutive cycle tests and long-term evaluations. This approach, combining crystalline modulation and interfacial engineering, presents a promising avenue for significantly boosting the electrocatalytic NITRR performance of metal nanoclusters under ambient conditions.

2. Experimental

2.1. Materials

$CuCl_2$ (Macklin, 98 %), $(CH_2OH)_2$ (Macklin, 98 %), NaOH (Macklin, 95 %), Multi-walled carbon nanotubes (MWCNTs, Damas-beta), Sodium citrate (Macklin, 99 %), Tannic acid (Damas-beta, 99 %), Ethylenediaminetetraacetic acid (General-Reagent, 99 %), Potassium sodium tartrate (Jinshan Chemical Reagent Co., Ltd.), C_2H_5OH (Jinshan Chemical Reagent Co., Ltd.), and Deionized (DI) water was used in all experiments.

2.2. Synthesis of a-Cu(OH)Cl/CNTs and c-$Cu_2(OH)_3Cl$/CNTs samples

Amorphous Cu(OH)Cl nanoclusters grown on carbon nanotubes (a-Cu(OH)Cl/CNTs) were synthesized by a simple and mild chelated co-precipitation method. Specifically, 0.2 g $CuCl_2$ and 25 mg CNTs were dispersed into 20 mL ethylene glycol (EG) to form a homogeneous suspension by ultrasonicated treatment for 30 min. 30 mg trisodium citrate dihydrate (TCD) was added into the above suspension under magnetic stirring. After that, 2 mL of 1 M NaOH solution was dropwise into the above suspension under magnetic stirring for 10 min, the obtained precipitate was rinsed with H_2O for three times and dried at 60 °C. The crystalline $Cu_2(OH)_3Cl$ nanoclusters grown on carbon nanotubes (c-$Cu_2(OH)_3Cl$/CNTs) sample was synthesized by the same preparation method as a-Cu(OH)Cl/CNTs, expect without the addition of TCD.

2.3. Synthesis of c-$Cu_2(OH)_3Cl$/CNTs-TA, c-$Cu_2(OH)_3Cl$/CNTs-EDTA and c-$Cu_2(OH)_3Cl$/CNTs-TART samples

The samples c-$Cu_2(OH)_3Cl$/CNTs-TA, c-$Cu_2(OH)_3Cl$/CNTs-EDTA and c-$Cu_2(OH)_3Cl$/CNTs-TART were synthesized using the identical preparation method employed for a-Cu(OH)Cl/CNTs, with the exception that 30 mg of TCD was substituted with 30 mg of tannic acid (TA), 30 mg of ethylenediaminetetraacetic acid (EDTA), and 30 mg of potassium sodium tartrate (TART), respectively.

3. Results and discussion

3.1. Preparation and characterization of samples

As depicted in Fig. 1a, the ultrafine a-Cu(OH)Cl nanoclusters, grown in situ on the surface of CNTs, were synthesized via a simple and gentle chelated co-precipitation method at ambient temperature. During the preparation process, TCD served as a crucial chelating agent, facilitating the formation of a-Cu(OH)Cl nanoclusters, featuring an average diameter of approximately 9 nm. Its significance lies in its ability to coordinate with Cu^{2+}, leading to the formation of a chelated precursor. This precursor then undergoes precipitation upon the addition of NaOH solution, ultimately resulting in the production of a-Cu(OH)Cl nanoclusters on the surface of CNTs (a-Cu(OH)Cl/CNTs). In the absence of TCD, the result-

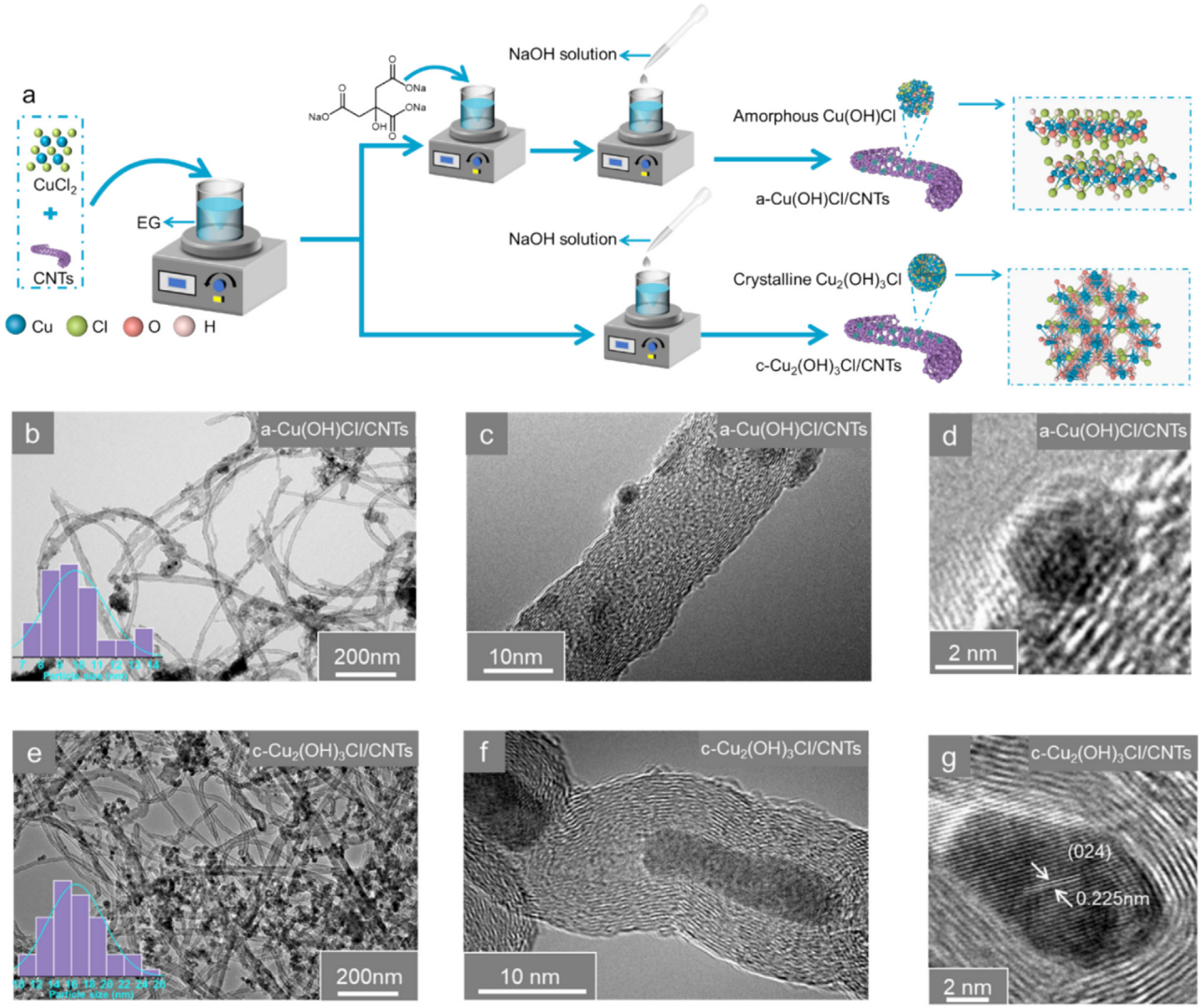

Fig. 1. (a) Schematic illustration of the synthesis routes for a-Cu(OH)Cl/CNTs and c-$Cu_2(OH)_3Cl$/CNTs samples. (b) TEM and (c, d) HR-TEM images of a-Cu(OH)Cl/CNTs. (e) TEM and (f, g) HR-TEM images of c-$Cu_2(OH)_3Cl$/CNTs. The insets in (b, e) show the corresponding particle size distribution histograms for a-Cu(OH)Cl/CNTs and c-$Cu_2(OH)_3Cl$/CNTs samples, respectively.

ing product was c-$Cu_2(OH)_3Cl$ nanoclusters, approximately 16.54 nm in average diameter, deposited on CNTs, designated as c-$Cu_2(OH)_3Cl$/CNTs. CNTs were chosen as the supporting skeleton material owing to their remarkable chemical stability, exceptional electrical conductivity, and abundant surface defects. Furthermore, metal ions exhibit strong interactions with the oxygen-containing species on the CNT surface, promoting the immobilization and dispersion of these Cu nanoclusters [39]. Transmission electron microscopy (TEM) was utilized to characterize the structural features of both a-Cu(OH)Cl/CNTs and c-$Cu_2(OH)_3Cl$/CNTs samples.

As depicted in Fig. 1b, e, the CNTs in these samples exhibit an intricate intertwining pattern, resulting in a three-dimensional conductive network structure. This configuration effectively facilitates the mass transfer and charge migration processes crucial for the electrochemical NITRR. As shown in Fig. 1b, the ultrafine a-Cu(OH)Cl nanoclusters exhibit a uniform distribution across the entire CNTs surface, with an average size distribution measuring approximately 9.69 nm, as depicted in the inset of Fig. 1b. Additionally, as shown in Fig. S1, the element mapping images of a-Cu(OH)Cl/CNTs, which revealed that Cu, Cl, and O elements are uniformly distributed over the a-Cu(OH)Cl nanoclusters loaded on the carbon nanotubes (CNTs). Furthermore, a thorough examination of a-Cu(OH)Cl/CNTs via high-resolution transmission electron microscopy (HR-TEM, Fig. 1c, d) reveals distinct lattice fringes of CNTs but no observable lattice fringes from Cu nanoclusters, indicating the amorphous nature of the Cu(OH)Cl nanoclusters. Interestingly, when without the addition of TCD while maintaining all other conditions identical to those employed for a-Cu(OH)Cl/CNTs, the obtained c-$Cu_2(OH)_3Cl$ nanoclusters exhibited a uniform distribution across the entire CNTs surface (Fig. 1e), with an average particle size (as shown in the inset of Fig. 1e) centered around 16.54 nm, significantly exceeding the size of a-Cu(OH)Cl nanoclusters. Moreover, the HR-TEM images (Fig. 1f, g) of the c-$Cu_2(OH)_3Cl$/CNTs sample reveal a distinct lattice spacing of 0.225 nm, corresponding to the (0 2 4) plane of $Cu_2(OH)_3Cl$ (Fig. 1g). The aforementioned results underscore the pivotal role of TCD in the formation of amorphous Cu nanoclusters. In addition, the incorporation of TCD leads to the formation of a-Cu(OH)Cl nanoclusters, exhibiting significantly reduced particle sizes compared to c-$Cu_2(OH)_3Cl$ nanoclusters. This reduction in size favorably contributes to the exposure of an increased number of catalytic sites during the electrocatalytic NITRR process.

X-ray powder diffraction (XRD) patterns of a-Cu(OH)Cl/CNTs and c-$Cu_2(OH)_3Cl$/CNTs are displayed in Fig. 2a. The XRD pattern of

c-$Cu_2(OH)_3Cl$/CNTs sample exhibits high crystallinity, featuring distinct diffraction peaks at 32.4°, 44.5°, 48.2°, 50.2°, 53.7°, 62.1°, and 67.9° corresponding to the (1 1 3), (0 2 4), (2 0 5), (0 3 3), (2 2 0), (2 1 7), and (2 2 6) planes of $Cu_2(OH)_3Cl$ (JCPDF card #87-0679). Conversely, the obtained a-Cu(OH)Cl/CNTs exhibits no discernible peaks associated with crystalline Cu nanoclusters, indicating the amorphous nature of the Cu(OH)Cl nanoclusters. The above observations provide further evidence that the incorporation of TCD is crucial for the formation of amorphous Cu nanoclusters, aligning well with the TEM analysis depicted in Fig. 1d, g. Additionally, Infrared spectra (IR) was carried out to explore the composition of samples (Fig. 2b). For the c-$Cu_2(OH)_3Cl$/CNTs sample, the absorption peaks situated at approximately 3450 and 3364 cm^{-1} are ascribed to the stretching vibrations of hydroxyl groups, which correspond to two distinct –OH environments characterized by varying atomic distances (d_{O-H}) and hydrogen bond angles ($\theta_{O-H\cdots Cl}$) [51]. In addition, the absorption peaks located at 989, 927 and 838 cm^{-1} could be attributed to the deformation modes of Cu—O—H in copper hydroxychlorides. However, when compared with c-$Cu_2(OH)_3Cl$/CNTs, only characteristic peak is observed at 3442 cm^{-1} in the a-Cu(OH)Cl/CNTs sample, suggesting the presence of O—H···Cl [52]. Besides, the surface compositions and element valence states of the samples were characterized utilizing X-ray photoelectron spectroscopy (XPS). According the analysis results of survey XPS spectra of samples (Fig. 2c), testify the existence of Cu, O and Cl, which is in according with the XRD (Fig. 2a) and IR (Fig. 2b) analysis results. As showed in Fig. 2d, the high-resolution XPS spectrum of the a-Cu(OH)Cl/CNTs and c-$Cu_2(OH)_3Cl$/CNTs catalyst in the Cu 2*p* region, which can be fitted with two peaks located at 932.4 and 935.2 eV, assigning to the Cu^{2+} and Cu^{+}, respectively. Furthermore, in the analysis of the XPS spectrum corresponding to the Cl 2*p* region, a peak is observed at approximately 199.8 eV which is consistent with the Cl—Cu bonding configuration. In the O 1*s* region, the deconvoluted peaks at binding energies of approximately 531.5, 532.3, and 533.2 eV are assigned to Cu—O, Cu—O—H and –OH of surface-absorbed water (Fig. S2). Based on the findings from the aforementioned analysis results, we inferred that the composition of the amorphous Cn nanocluster was Cu(OH)Cl (Fig. S3) [52]. To gain a more profound comprehension of the amorphous Cu cluster's formation mechanism, we conducted a series of spectroscopic analyses, as depicted in Fig. 2e, f. As shown in Fig. 2e, in contrast to TCD and $CuCl_2$ solution, the mixture of TCD and $CuCl_2$ solution exhibited new characterized peaks, which could potentially be attributed to the formation of the chelated $Cu_x(C_6H_5O_7)_3$ precursor, leading to a new coordination environment. Meanwhile, in Fig. 2f, the absorbance of the mixture solution greatly improved and occurred blue shift. Furthermore, the inset of Fig. 2f clearly demonstrates a pronounced color alteration upon mixing the $CuCl_2$ and TCD solutions. The aforementioned phenomena indicate the occurrence of a chelation reaction between Cu^{2+} and TCD, resulting in the formation of a chelate. Drawing from the aforementioned analyses, we deduce that the negatively charged $-COO^-$ groups present in TCD exhibit a propensity to interact with positively charged Cu^{2+}, leading to the construction of a $Cu_x(C_6H_5O_7)_2$ chelate. The formation of these chelates modifies the nucleation behavior of the Cu-precursors during the subsequent NaOH precipitation stage, ultimately facilitating the generation of an amorphous Cu nanocluster. Moreover, the modulation of the crystalline structure of Cu nanoclusters may be related to the unique chemical structure of TCD. For example, we conducted control experiments using tannic acid (TA), ethylenediaminetetraacetic acid (EDTA), or potassium sodium tartrate (TART) as chelating agents for comparison. As shown in Figs. S4 and S5, the addition of either TA, EDTA, or TART facilitates the in situ growth of ultrafine high-crystallinity $Cu_2(OH)_3Cl$ nanoclusters on the surface of CNTs, achieving the preparation of c-$Cu_2(OH)_3Cl$/CNTs-TA, c-$Cu_2(OH)_3Cl$/CNTs-EDTA, and c-$Cu_2(OH)_3Cl$/CNTs-TART samples, respectively. However, unlike the effect observed with TCD as a chelating agent, the incorporation of TA, EDTA, or TART does not

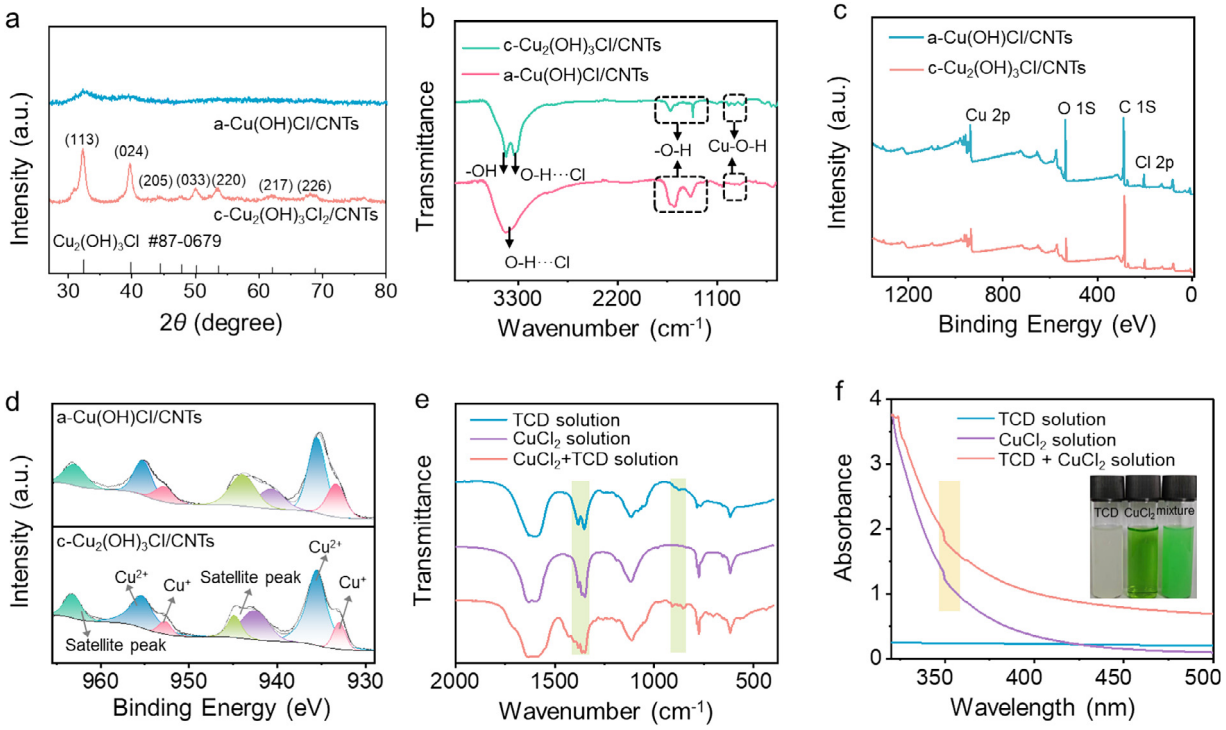

Fig. 2. (a) XRD patterns of a-Cu(OH)Cl/CNTs and c-$Cu_2(OH)_3Cl$/CNTs samples. (b) Infrared spectra of a-Cu(OH)Cl/CNTs and c-$Cu_2(OH)_3Cl$/CNTs samples. (c) Survey XPS profiles and (d) high-resolution XPS spectra at the Cu 2*p* region of a-Cu(OH)Cl/CNTs and c-$Cu_2(OH)_3Cl$/CNTs samples. (e) Infrared spectra and (f) UV–vis absorption spectra of $CuCl_2$ solution, TCD solution, and the mixture of $CuCl_2$ and TCD solution.

modify the crystallographic structure of the Cu-based nanoclusters. Specifically, when using TA, EDTA, or TART as chelating agents, the resultant nanoclusters are high-crystallinity $Cu_2(OH)_3Cl$ nanoclusters (Fig. S4). The aforementioned results indicate that the addition of chelating agents, such as TA, EDTA, and TART, favors the in situ growth of crystalline $Cu_2(OH)_3Cl$ nanoclusters with extremely small particle sizes on the surface of CNTs. However, only TCD promotes the growth of amorphous Cu(OH)Cl nanoclusters.

The chemical states and coordination environments of the a-Cu(OH)Cl/CNTs and c-$Cu_2(OH)_3Cl$/CNTs samples were investigated using the techniques of X-ray absorption near-edge structure (XANES) and extended X-ray absorption fine structure (EXAFS). Fig. 3a shows that the absorption edge profiles for both a-Cu(OH)Cl/CNTs and c-$Cu_2(OH)_3Cl$/CNTs are close to that of CuO, indicating the valence state of Cu species approximates to +2. As depicted in Fig. 3b, the extended X-ray absorption fine structure (EXAFS) spectra of the Cu K-edge for a-Cu(OH)Cl/CNTs and c-$Cu_2(OH)_3Cl$/CNTs samples exhibited a prominent peak at 1.97 Å, corresponding to the Cu—O bond, which is similar to standard sample of Cu_2O and CuO. Additionally, a more in-depth analysis of the quantitative coordination structure of the Cu atoms can be achieved through the fitting of the k^3-weighted Fourier transform EXAFS spectra, as depicted in Fig. 3c–f, Fig. S6 and Table S1. In the composite of a-Cu(OH)Cl/CNTs, the coordination number (CN) surrounding the Cu atoms approximates 5, significantly lower than the CN of ~8 observed in c-$Cu_2(OH)_3Cl$/CNTs, as detailed in Table S1. This distinct feature suggests that the surface of the a-Cu(OH)Cl cluster in a-Cu(OH)Cl/CNTs contains a greater abundance of low-coordination Cu atoms, thereby offering an increased number of catalytic sites for electrochemical NITRR. It is worth noting that, when compared to CNTs and c-$Cu_2(OH)_3Cl$/CNTs samples, a-Cu(OH)Cl/CNTs catalyst demonstrate a more pronounced surface defect signal (Fig. 3g). This is potentially due to the abundance of low-coordination Cu atoms located on the surface of the a-Cu(OH)Cl nanocluster (Fig. 3g). Furthermore, as illustrated in Fig. 3h–l, the wavelet transforms (WT) plots of the Cu K-edge Fourier transform EXAFS for a-Cu(OH)Cl/CNTs and c-$Cu_2(OH)_3Cl$/CNTs samples exhibits a distinct intensity peak centered around 6.1 $Å^{-1}$. This peak is indicative of the Cu—O interaction, thus affirming that the predominant Cu state on both a-Cu(OH)Cl/CNTs and c-$Cu_2(OH)_3Cl$/CNTs catalysts is in the oxidation state.

3.2. Electrochemical nitrate reduction performances

All electrochemical experiments were conducted on a standard two-compartment cell separated by a Nafion-117 proton exchange membrane (Fig. S7). For preliminary investigation, the catalytic activities of a-Cu(OH)Cl/CNTs and c-$Cu_2(OH)_3Cl$/CNTs for the NITRR, linear sweep voltammetry (LSV) curves of samples were performed in 0.1 M Na_2SO_4 solution and 0.1 M Na_2SO_4 containing 500 ppm NO_3^- solution, respectively, at room temperature. As depicted in Fig. 4a, within the potential range from −0.7 to −1.1 V versus reversible hydrogen electrode (vs RHE), the current density of a-Cu(OH)Cl/CNTs and c-$Cu_2(OH)_3Cl$/CNTs samples in a 0.1 M Na_2SO_4 solution with 500 ppm NO_3^- is significantly greater than that in a 0.1 M Na_2SO_4 solution alone. This indicates the possible occurrence of the NITRR in the Na_2SO_4 solution containing NO_3^-. In order to delve deeper into the catalytic performance of a-Cu(OH)Cl/CNTs and c-$Cu_2(OH)_3Cl$/CNTs samples, NITRR tests were conducted at varying applied potentials ranging from −0.7 to −1.1 V (vs RHE). After a 10-min chronoamperometry test (Fig. S8a, b), the potential presence of ammonia product in the electrolyte solution within the cathode compartment was quantitatively analyzed using the indophenol blue method. Fig. S8c, d display the ultraviolet–visible (UV–vis) absorption spectra of the product solutions stained with the indophenol blue indicator. Fig. S9a shows the UV–vis absorption spectra of the standard ammonia solution at different concentrations, along with the corresponding calibration curves (Fig. S9b). Fig. S9b demonstrates a strong linear correlation between light absorbance at a wavelength of 665 nm and the concentration of ammonia. Based on the NH_3 standard curve calibration (Fig. S9b), the NH_3 yield (Fig. 4b) and corresponding FE_{NH3} (Fig. 4c) of the a-Cu(OH)Cl/CNTs and c-$Cu_2(OH)_3Cl$/CNTs catalyst at various potentials were calculated. The a-Cu(OH)Cl/CNTs catalyst showed its highest NH_3 yield and FE_{NH3} at −0.9 V vs RHE, achieving values of 342.70 μg h^{-1} $mg_{cat.}^{-1}$ and 80.2 %, respectively, are obviously higher than that of c-$Cu_2(OH)_3Cl$/CNTs catalyst (159.23 μg h^{-1} $mg_{cat.}^{-1}$ and 62.1 %, respectively, at −0.9 V vs RHE). Moreover, the NH_3 yield and FE_{NH3} of a-Cu(OH)Cl/CNTs are significantly higher than those of c-$Cu_2(OH)_3Cl$/CNTs across a broad potential range (from −0.7 to −1.1 V). The analysis results above indicate a significantly higher catalytic activity of a-Cu(OH)Cl/CNTs in the NITRR when compared to c-$Cu_2(OH)_3Cl$/CNTs. This may be attributed to the fact that the addition of TCD can lead to the formation of amorphous Cu nanoclusters, which provide more catalytic activity sites on the surface of the a-Cu(OH)Cl/CNTs catalyst compared to the c-$Cu_2(OH)_3Cl$/CNTs catalyst. To verify a-Cu(OH)Cl/CNTs exposed exhibited a higher number of active sites on its surface, cyclic voltammetry (CV) curves of various samples were compared across different scan rates within the non-Faradaic current potential range (Fig. S10). The double-layer capacitance (C_{dl}) values for a-Cu(OH)Cl/CNTs (0.81 mF cm^{-2}) and c-$Cu_2(OH)_3Cl$/CNTs (0.45 mF cm^{-2}) were determined by plotting the corresponding anodic charging currents linearly against the scan rates at the open-circuit potential. Based on the aforementioned analysis results, we computed the electrochemically active surface area (ECSA). It is evident that a-Cu(OH)Cl/CNTs exhibits a larger ECSA (20.25 cm^2) than c-$Cu_2(OH)_3Cl$/CNTs, which has an ECSA of 10.25 cm^2. Furthermore, as illustrated in Fig. S11, the specific activity of catalyst was also calculated as the NH_3 yield normalized to the ECSA of each sample. The specific activity of a-Cu(OH)Cl/CNTs is found to be 6.77 μg h^{-1} cm^{-2} at −0.9 V vs RHE, significantly surpassing that of c-$Cu_2(OH)_3$/CNTs, which stands at 6.40 μg h^{-1} cm^{-2} under the same potential condition. This indicates that a-Cu(OH)Cl/CNTs possess more efficient catalytic sites compared to c-$Cu_2(OH)_3$/CNTs. Moreover, the smaller particle size of Cu-based nanoclusters facilitates the exposure of catalytically active sites, thereby effectively enhancing the performance of NITRR. For instance, the particle sizes of high-crystallinity $Cu_2(OH)_3Cl$ nanoclusters within the c-$Cu_2(OH)_3Cl$/CNTs-TA sample (featuring a diameter of approximately 7.9 nm, Fig. S4b) and the c-$Cu_2(OH)_3Cl$/CNTs-EDTA sample (with a diameter of roughly 3.56 nm, Fig. S4e) are significantly reduced compared to those observed in the c-$Cu_2(OH)_3Cl$/CNTs sample (which exhibits a diameter of approximately 16.54 nm, Fig. 1e). Consequently, as shown in Fig. S12, the NITRR selectivity of c-$Cu_2(OH)_3Cl$/CNTs-TA and c-$Cu_2(OH)_3Cl$/CNTs-EDTA is significantly enhanced compared to that (Fig. 4c) of c-$Cu_2(OH)_3Cl$/CNTs. As listed in Table S2, the catalytic performance of a-Cu(OH)Cl/CNTs is competitive when compared to recently reported electrocatalysts for the NITRR, even when utilizing an extremely low concentration (500 ppm) of NO_3^- as the nitrogen source. As depicted in Fig. S13, as the concentration of NO_3^- increases, the NH_3 yield exhibits a continuous rise. Moreover, within the range of NO_3^- concentrations (from 100 to 1500 ppm) considered, the FE_{NH3} remains consistently above 75 %. It is noteworthy that a-Cu(OH)Cl/CNTs exhibits a FE_{NH3} of approximately 80 % in electrolyte solutions containing extremely low concentrations (such as 100 and 250 ppm) of NO_3^-. Given that wastewater may contain a high-salt environment, it is crucial to examine the catalytic performance of the a-Cu(OH)Cl/CNTs catalyst under high-salt concentration condition. As illustrated in Fig. S14, when the concentration of Na_2SO_4 ranges from 0.1 to 2 M, the FE_{NH3} of the a-Cu(OH)Cl/CNTs catalyst remains above 75 %. The aforementioned analysis results indicate that the a-Cu(OH)Cl/CNTs

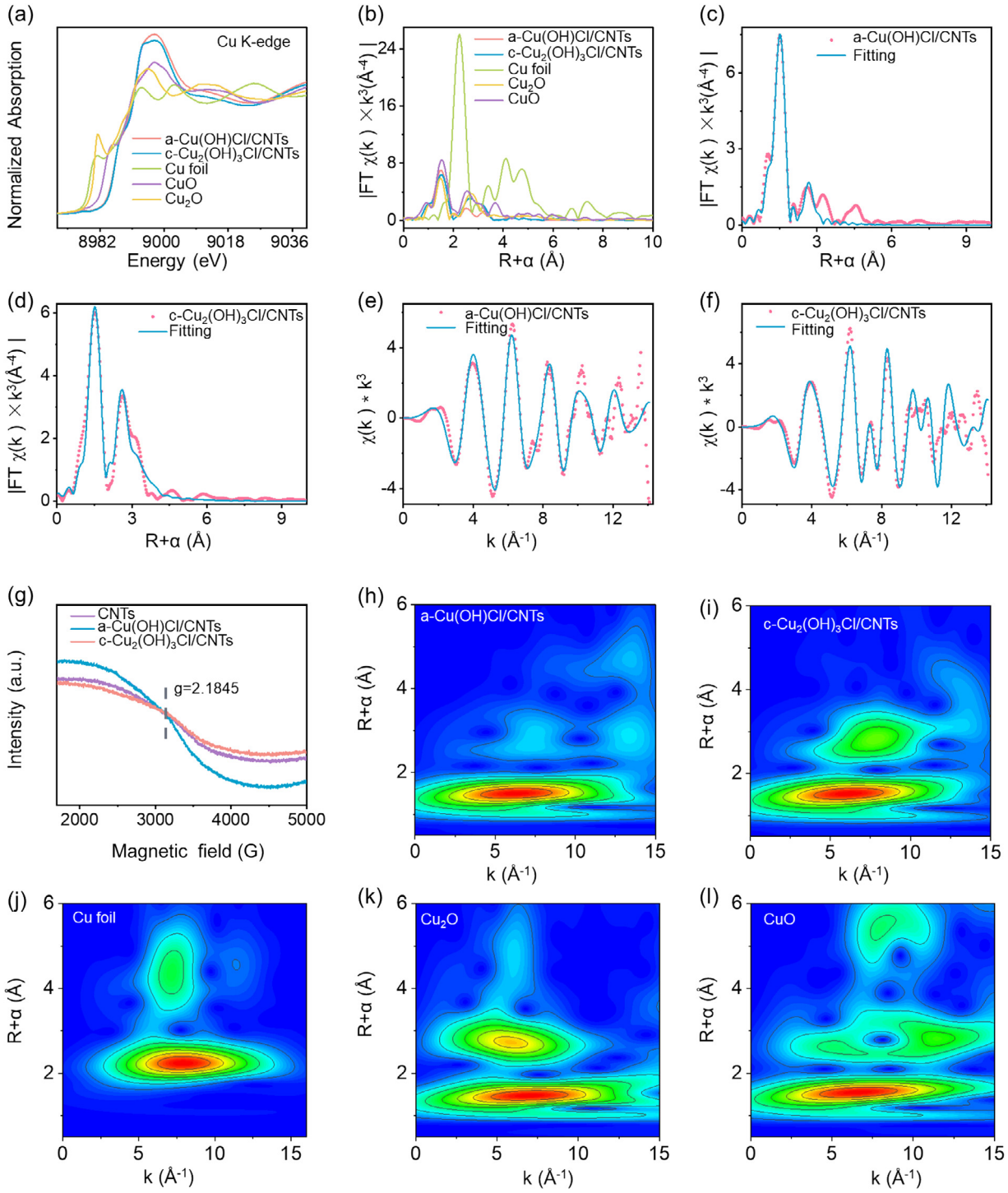

Fig. 3. (a) Cu K-edge XANES spectra of a-Cu(OH)Cl/CNTs, c-$Cu_2(OH)_3Cl$/CNTs, Cu foil, Cu_2O and CuO samples. (b) Fourier transformations of the k_3-weighted $\chi(k)$-function of the EXAFS spectra at Cu K-edge of a-Cu(OH)Cl/CNTs, c-$Cu_2(OH)_3Cl$/CNTs, Cu foil, Cu_2O and CuO samples. Fitting results of the EXAFS spectra of a-Cu(OH)Cl/CNTs and c-$Cu_2(OH)_3Cl$/CNTs at *R* space (c, d) and *k*-space (e, f). (g) Electron paramagnetic resonance (EPR) spectra of CNTs, a-Cu(OH)Cl/CNTs and c-$Cu_2(OH)_3Cl$/CNTs samples. WT of the Cu K-edge FT-EXAFS spectra of (h) a-Cu(OH)Cl/CNTs, (i) c-$Cu_2(OH)_3Cl$/CNTs, (j) Cu foil, (k) Cu_2O, and (l) CuO.

catalyst exhibits favorable performance under actual wastewater testing conditions, such as low-concentration nitrate wastewater or high-salt environments. As presented in Fig. 4d, the Nyquist plots of all the samples were fitted with a standard equivalent circuit (inset in Fig. 4d.) This fitting was carried out to determine the values of the charge-transfer resistance (R_{ct}). It is worth noting that the equivalent series resistance values for the a-Cu(OH)Cl/CNTs (5.79 Ω), are considerably lower than those of the c-$Cu_2(OH)_3Cl$/CNTs (11.58 Ω). This finding implies that a-Cu(OH)Cl/CNTs electrode possesses lower R_{ct} values and demonstrate faster catalytic kinetics when compared to a-$Cu_2(OH)_3Cl$/CNTs electrode.

Apart from the NH_3 product, the possible by-product, such as NO_2^- in the electrolyte solution was detected by the Griess method. Fig. S15a shows the UV–vis absorption spectra of the standard NO_2^- solution at different concentrations, along with the corresponding calibration curves (Fig. S15b). As shown in Fig. 4e and Fig. S16,

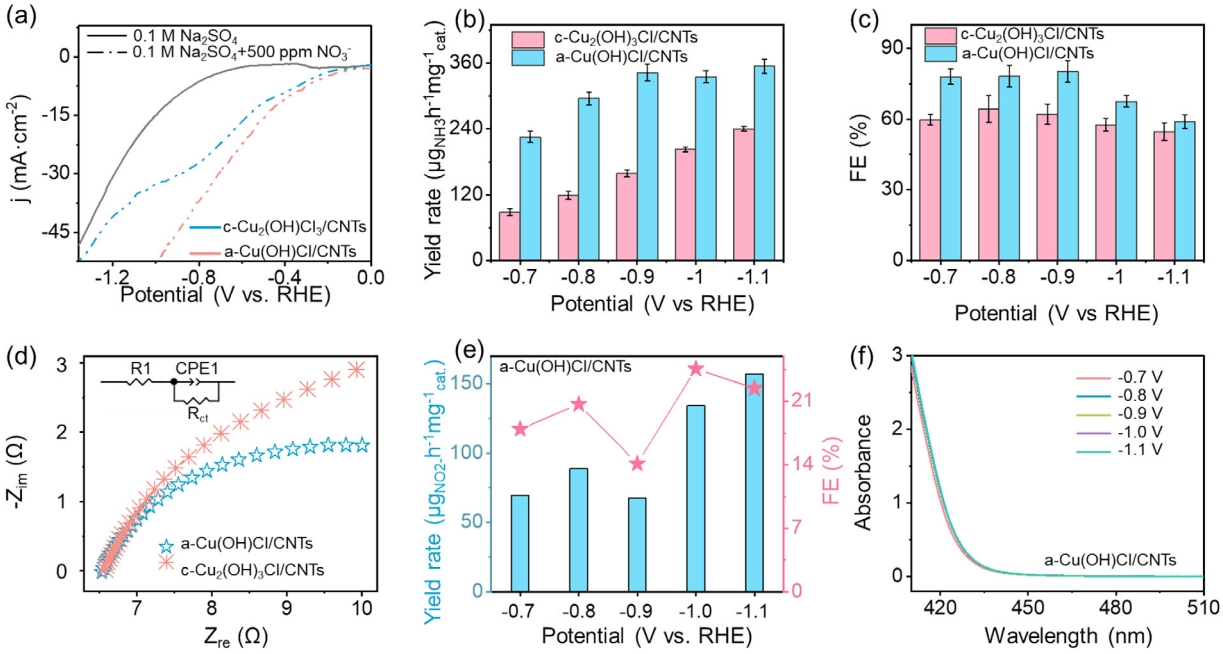

Fig. 4. (a) LSV curves of a-Cu(OH)Cl/CNTs and c-$Cu_2(OH)_3Cl$/CNTs measured in 0.1 M Na_2SO_4 solution with or without 500 ppm of NO_3^-, respectively. (b) The NH_3 yield and (c) corresponding FE_{NH3} values of a-Cu(OH)Cl/CNTs and c-$Cu_2(OH)_3Cl$/CNTs at different applied potentials for electrochemical NITRR. (d) Nyquist plots of a-Cu(OH)Cl/CNTs and c-$Cu_2(OH)_3Cl$/CNTs measured at −0.9 V vs RHE in 0.1 M Na_2SO_4 solution containing 500 ppm of NO_3^-. (e) The NO_2^- yields and corresponding FE values for a-Cu(OH)Cl/CNTs at given potentials for the NITRR. (f) UV–Vis absorption spectra of the 0.1 M Na_2SO_4 + 500 ppm NO_3^- solution after the NITRR test of a-Cu(OH)Cl/CNTs for 10 min at various applied potentials and then coloured by the *para*-dimethylamino-benzaldehyde indicator.

compared with a-Cu(OH)Cl/CNTs, c-$Cu_2(OH)_3Cl$/CNTs exhibits a higher and more efficient conversion of NO_3^- to NO_2^-, which is a rate-limiting step in the electrochemical reduction process that transforms NO_3^- into NH_3 [18]. It is evident that a-Cu(OH)Cl/CNTs could effectively facilitate the subsequent reduction of NO_2^- to NH_3. Additionally, the Watt and Chrisp method (Fig. S17) was used to detect a possible byproduct N_2H_4. Fig. 4f demonstrates that no N_2H_4 was detected in the experiment. The above analysis results indicate that a-Cu(OH)Cl/CNTs has high selectivity for the electrochemical NITRR to NH_3. Similarly, the primary liquid-phase byproduct observed in the electrocatalytic NITRR process utilizing c-$Cu_2(OH)_3Cl$/CNTs as the electrocatalyst, with no detectable presence of N_2H_4 (Fig. S18). To rule out the possibility of ammonia contamination from the catalyst itself or external environmental sources, we conducted a series of comparative experiments (Fig. 5a) at the optimal potential of –0.9 V vs RHE. Initially, the a-Cu(OH)Cl/CNTs material was subjected to electrolysis in a 0.1 M Na_2SO_4 solution without NO_3^- at –0.9 V vs RHE, and no ammonia production was detected. In a subsequent control experiment, the a-Cu(OH)Cl/CNTs catalyst was electrolyzed in a 0.1 M Na_2SO_4 solution with 500 ppm of NO_3^- at the open-circuit potential (OCP), yet it did not yield a measurable quantity of NH_3. Furthermore, after conducting chronoamperometry tests using bare carbon paper (CP) as the working electrode in a 0.1 M Na_2SO_4 solution with 500 ppm NO_3^- at –0.9 V vs RHE, no NH_3 was produced. Moreover, Fig. S19 shows that the NH_3 yield of 342.69 μg h^{-1} $mg_{cat.}^{-1}$ for a-Cu(OH)Cl/CNTs at –0.9 V vs RHE is obviously higher than that of pristine CNTs (55.02 μg h^{-1} $mg_{cat.}^{-1}$), suggesting that the ultrafine amorphous Cu(OH)Cl nanoclusters are the main active sites during the NITRR. More importantly, a ^{15}N isotope-labeling experiment was conducted by administering $^{15}NO_3^-$ ($Na^{15}NO_3$ with 98.3 % enrichment, Sigma). As depicted in Fig. 5b, the ^1H NMR spectra of the electrolyte following 0.5 h of electrocatalytic reduction of $^{15}NO_3^-$ exhibited the characteristic double peaks of $^{15}NH_4^+$, whereas when utilizing $^{14}NO_3^-$ as the primary nitrogen source, only $^{14}NH_4^+$ with a triplet coupling peak was observed. This further validates that the ammonia generated during the electrolysis tests with a-Cu(OH)Cl/CNTs originated solely from the reduction of NO_3^-.

Stability stands as a pivotal criterion in the assessment of electrocatalyst performance. Hence, we examined the stability of the a-Cu(OH)Cl/CNTs sample for electrocatalytic NITRR in a 0.1 M Na_2SO_4 solution with 500 ppm NO_3^-. As shown in Fig. 5c, the outcomes from 10 successive cyclic trials of a-Cu(OH)Cl/CNTs reveal no significant alterations in the ammonia production rate and FE, where the ammonia yield and FE were higher than 300 μg h^{-1} $mg_{cat.}^{-1}$ and 70 % respectively, suggesting the good stability of a-Cu(OH)Cl/CNTs catalyst during NITRR. Furthermore, the long-term durability of the a-Cu(OH)Cl/CNTs catalyst was evaluated over a 24-h period. As depicted in Fig. 5d, the catalyst was able to sustain a selectivity of over 70 % even after the prolonged test, which underscores its remarkable stability. In addition, the time-dependent concentration of NO_3^- and NO_2^- in the electrolyte solution during the NITRR was measured (Figs. S20 and S21). As illustrated in Fig. S21a, the concentration of NO_3^- exhibits a gradual decline with the extension of electrocatalytic test duration. Meanwhile, the NO_2^- concentration first rose and then fell. This phenomenon may be attributed to the fact that in the NITRR process, NO_3^- is first reduced to NO_2^-, followed by the subsequent reduction of NO_2^- to NH_3. It is noteworthy that after conducting a 4-h electrocatalytic NITRR test on the a-Cu(OH)Cl/CNTs catalyst at –0.9 V vs. RHE in a 0.1 M Na_2SO_4 solution containing 500 ppm of NO_3^-, the measured concentrations of NO_3^- and NO_2^- in the solution were 20.2 and 2.1 μg mL^{-1}, respectively. These concentrations were below the limits set by the World Health Organization (WHO) for NO_3^- (50 μg mL^{-1}) and NO_2^- (3 μg mL^{-1}) in drinking water [53,54]. Moreover, after 4 h of electrocatalytic testing, a removal rate of approximately 96.0 % is attained (Fig. S21b). This result suggests that the a-Cu(OH)Cl/CNTs catalyst is capable of efficiently and promptly eliminating nitrate from aqueous solutions, even when a relatively low nitrate concentration (500 ppm) is employed as the

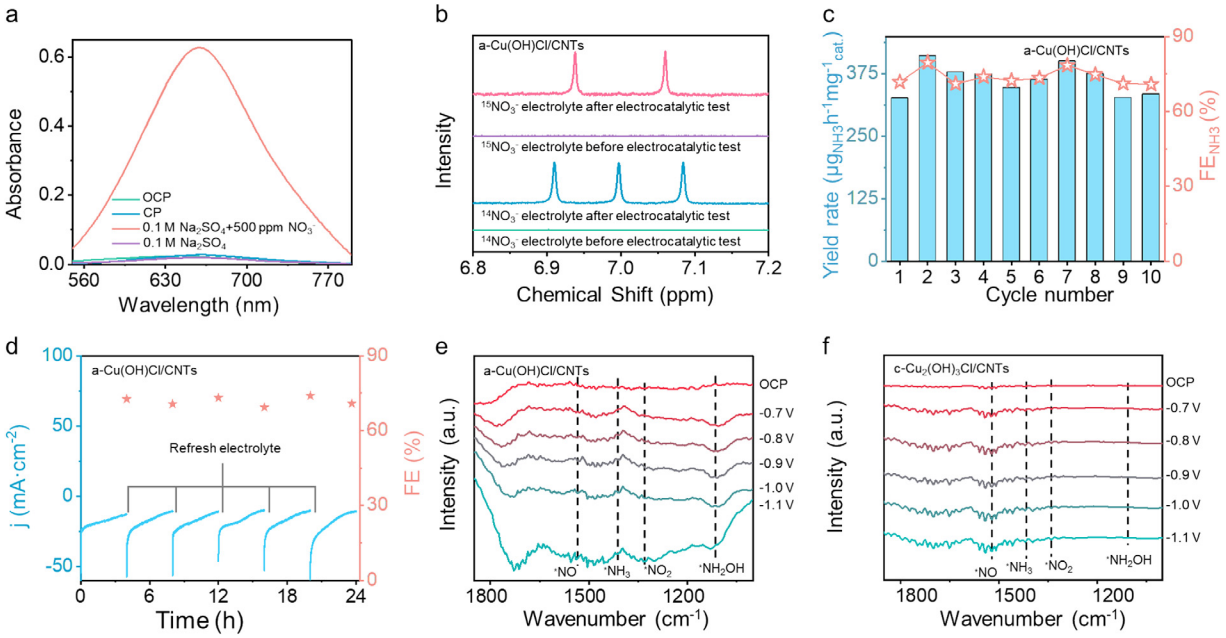

Fig. 5. (a) UV–vis absorption spectra after 10 min of electrolysis at –0.9 V vs RHE for a-Cu(OH)Cl/CNTs under different conditions and coloured with indophenol indicator. (b) ^{1}H NMR spectra of the electrolyte after the NITRR test of a-Cu(OH)Cl/CNTs using $^{15}NO_3^-$ and $^{14}NO_3^-$ as the N-sources, respectively. (c) Cycling stability of a-Cu(OH)Cl/CNTs for the NITRR during 10 cycles at –0.9 V vs RHE. (d) The corresponding time-dependent current density curves of long-term stability tests and corresponding FE_{NH3} after a-Cu(OH)Cl/CNTs at a potential of –0.9 V vs RHE. In-situ infrared spectra of (e) a-Cu(OH)Cl/CNTs and (f) c-$Cu_2(OH)_3Cl$/CNTs samples at different negative applied potentials in the 0.1 M Na_2SO_4 electrolytes containing 500 ppm NO_3^-.

nitrogen source. Furthermore, 100 consecutive cyclic voltammetry (CV) tests were executed to evaluate the stability of the a-Cu(OH)Cl/CNTs sample. As shown in Fig. S22a, the CV curves of the a-Cu(OH)Cl/CNTs in a 0.1 M Na_2SO_4 solution, recorded at a scan rate of 100 mV s^{-1}, exhibit no discernible redox peaks, indicating that Cl^- remains stable under electrolytic conditions. Moreover, the elemental amount of the a-Cu(OH)Cl/CNTs catalyst, including elements such as Cl, Cu, and C, was compared before and after undergoing electrocatalytic stability testing for NITRR (Fig.S22b). As listed in Table S3, the Cl, Cu, and C content in the a-Cu(OH)Cl/CNTs catalyst exhibited no significant change before and after the stability testing, suggesting the remarkable compositional and structural stability of the a-Cu(OH)Cl/CNTs sample during the electrochemical NITRR for NH_3 synthesis. Additionally, we conducted an analysis of the Cu 2*p* region in a-Cu(OH)Cl/CNTs following the electrocatalytic stability test. As depicted in Fig. S23, there was no significant alteration in the valence state of the Cu species. This demonstrates the effective stabilizing effect of inorganic ligands (e.g., OH^- and Cl^-) on copper-based nanoclusters.

3.3. Exploration of electrocatalytic NITRR mechanism

To gain a deeper understanding of the NO_3RR process on a-Cu(OH)Cl/CNTs and c-$Cu_2(OH)_3Cl$/CNTs, in situ Fourier Transform Infrared (FTIR) spectroscopy was employed to identify potential intermediates. As shown in Fig. 5e, f, the characteristic absorption peak of 1329 cm^{-1} [55] was attributed to the asymmetric stretching vibration of N=O, manifesting NO_3^- was reduced to $*NO_2$, and further deoxygenation forming *NO (1530 cm^{-1}) [12] species on the surface of a-Cu(OH)Cl/CNTs. With the emergence of deoxidation intermediates, the hydrogenation intermediates, especially $*NH_2OH$ was consequently observed at 1120 cm^{-1}, indicating the reduction reaction is a continuous process of deoxidation and hydrogenation [16,25]. Ultimately, NO_3^- underwent electrocatalytic reduction, resulting in the generation of NH_3, which was detected at a wavenumber of 1419 cm^{-1} [55]. Accordingly, the presumed primary pathway for the reduction reaction is $*NO_3^- \rightarrow *NO_2^- \rightarrow *NO \rightarrow *NH_2OH \rightarrow NH_3$. Moreover, compared to the in situ FTIR spectroscopy of a-Cu(OH)Cl/CNTs, the intensity of the distinct absorption peaks for the aforementioned key intermediates observed on the surface of the c-$Cu_2(OH)_3Cl$/CNTs sample shows a noticeable weakening. This indicates that a-Cu(OH)Cl/CNTs is more conducive to the absorption and transformation of reactive intermediates during the NITRR process. This may be attributed to the smaller particle size of a-Cu(OH)Cl nanoclusters and the presence of low-coordination Cu atoms on their surface, which are more favorable for the adsorption and activation of reactive intermediates [25,39,49]. Consequently, this facilitates the conversion of nitrate into ammonia through a multi-step proton-coupled electron transfer process. Hence, compared to c-$Cu_2(OH)_3Cl$/CNTs, a-Cu(OH)Cl/CNTs demonstrates superior electrocatalytic performance. The results obtained from in situ FTIR spectroscopy are in agreement with the performance tests conducted for the electrocatalytic NITRR.

4. Conclusions

In summary, we report in situ growth of ultrafine amorphous Cu(OH)Cl nanoclusters, exhibiting a uniform diameter of roughly 9 nm, onto CNTs utilizing a simple and convenient chelated co-precipitation method. In this process, TCD acts as a chelating agent, promoting the formation of amorphous Cu(OH)Cl nanoclusters rather than crystalline $Cu_2(OH)_3Cl$ nanoclusters. Compared to crystalline $Cu_2(OH)_3Cl$ nanoclusters, the amorphous Cu(OH)Cl nanoclusters feature a surface rich in low-coordination Cu atoms, offering more active sites to enhance the electrochemical NITRR performance. Additionally, the introduction of TCD results in the formation of amorphous Cu(OH)Cl clusters with a significantly smaller particle size compared to crystalline $Cu_2(OH)_3Cl$ clusters, which further favorably contributes to the exposure of an increased number of catalytic sites during the electrocatalytic NITRR process. As a result, the resulting amorphous Cu(OH)Cl nan-

oclusters have more catalytically active sites and better activity than crystalline $Cu_2(OH)_3Cl$ catalysts. This study offers fresh perspectives on the crystalline modulation engineering of metal nanoclusters, aimed at enhancing electrocatalytic renewable energy conversion reactions.

CRediT authorship contribution statement

Xi Chen: Writing – review & editing, Writing – original draft, Software, Methodology, Investigation, Formal analysis, Data curation. **Fasheng Chen:** Software, Formal analysis, Data curation. **Xin-yu Zhong:** Software, Resources. **Junjie Ding:** Resources. **Huaizhu Wang:** Resources. **Liwen Dai:** Data curation. **Xinchuan Ma:** Formal analysis. **Hui Wang:** Resources. **Chang Wu:** Formal analysis. **Xiao Li:** Supervision, Resources. **Yan Xiong:** Software, Resources. **Zhong Jin:** Writing – review & editing, Visualization, Supervision, Resources, Project administration, Funding acquisition. **Minghang Jiang:** Writing – review & editing, Writing – original draft, Validation, Supervision, Resources, Project administration, Funding acquisition, Formal analysis, Conceptualization.

Declaration of competing interest

The authors declare that they have no known competing financial interests or personal relationships that could have appeared to influence the work reported in this paper.

Acknowledgments

The authors appreciate the financial support from the National Natural Science Foundation of China (22479074 and 22475096), the Natural Science Foundation of Sichuan Province (2023NSFSC1074 and 2025NSFTD0005), the Talent Introduction Plan of Xihua University (Z222051), the Equipment Pre-Research and MOE Joint Fund General Project (8091B02052407), the National Science Foundation of Jiangsu Province (BK20240400 and BK20241236), the Jiangsu Province Science and Technology Major Project (BG2024013), the Jiangsu Province Scientiflc and Technological Achievenments Transformation Special Fund (BA2023037), the Jiangsu Province Academic Degree and Postgraduate Education Reform Project (JGKT24_C001), the Suzhou City Key Core Technology Open Competition Project (SYG2024122), the Open Research Fund of Suzhou Laboratory (SZLAB-1308-2024-TS005), the Suzhou City Gusu Leading Talent Program of Scientific and Technological Innovation and Entrepreneurship (ZXL2021273), and the Chenzhou National Sustainable Development Agenda Innovation Demonstration Zone Provincial Special Project (2023sfq11).

Appendix A. Supplementary material

Supplementary data to this article can be found online at https://doi.org/10.1016/j.jechem.2025.07.017.

References

[1] M. Jiang, X. Chen, F. Chen, M. Wang, X. Luo, Y. He, C. Wu, L. Zhang, X. Li, X. Liao, Z. Jiang, Z. Jin, Chem 11 (2025) 102441.
[2] M. Jiang, L. Han, P. Peng, Y. Hu, Y. Xiong, C. Mi, Z. Tie, Z. Xiang, Z. Jin, Nano Lett. 22 (2021) 372–379.
[3] Y. Xiong, B. Li, Y. Gu, T. Yan, Z. Ni, S. Li, J.-L. Zuo, J. Ma, Z. Jin, Nat. Chem. 15 (2022) 286–293.
[4] X. Xue, H. Chen, Y. Xiong, R. Chen, M. Jiang, G. Fu, Z. Xi, X.L. Zhang, J. Ma, W. Fang, Z. Jin, ACS Appl. Mater. Interfaces 13 (2021) 4975–4983.
[5] R.-T. Gao, Z. Gao, N.T. Nguyen, J. Chen, X. Liu, L. Wang, L. Wu, Nat. Sustain. 8 (2025) 672–681.
[6] Y. Wang, M. Sun, J. Zhou, Y. Xiong, Q. Zhang, C. Ye, X. Wang, P. Lu, T. Feng, F. Hao, F. Liu, J. Wang, Y. Ma, J. Yin, S. Chu, L. Gu, B. Huang, Z. Fan, Proc. Natl. Acad. Sci. U.S.A. 120 (2023) e2306461120.
[7] X. Xue, R. Chen, H. Chen, Y. Hu, Q. Ding, Z. Liu, L. Ma, G. Zhu, W. Zhang, Q. Yu, J. Liu, J. Ma, Z. Jin, Nano Lett. 18 (2018) 7372–7377.
[8] J. Li, G. Zhan, J. Yang, F. Quan, C. Mao, Y. Liu, B. Wang, F. Lei, L. Li, A.W.M. Chan, L. Xu, Y. Shi, Y. Du, W. Hao, P.K. Wong, J. Wang, S.-X. Dou, L. Zhang, J.C. Yu, J. Am. Chem. Soc. 142 (2020) 7036–7046.
[9] M. Jiang, Q. Zhu, X. Song, Y. Gu, P. Zhang, C. Li, J. Cui, J. Ma, Z. Tie, Z. Jin, Environ. Sci. Technol. 56 (2022) 10299–10307.
[10] X. Xue, R. Chen, C. Yan, P. Zhao, Y. Hu, W. Zhang, S. Yang, Z. Jin, Nano Res. 12 (2019) 1229–1249.
[11] P. Li, L. Liao, Z. Fang, G. Su, Z. Jin, G. Yu, Proc. Natl. Acad. Sci. U.S.A. 120 (2023) e2305489120.
[12] S. Han, H. Li, T. Li, F. Chen, R. Yang, Y. Yu, B. Zhang, Nat. Catal. 6 (2023) 402–414.
[13] H. Xu, Y. Ma, J. Chen, W.-X. Zhang, J. Yang, Chem. Soc. Rev. 51 (2022) 2710–2758.
[14] M. Jiang, H. Wang, M. Zhu, X. Luo, Y. He, M. Wang, C. Wu, L. Zhang, X. Li, X. Liao, Z. Jiang, Z. Jin, Chem. Soc. Rev. 53 (2024) 5149–5189.
[15] M. Jiang, M. Zhu, M. Wang, Y. He, X. Luo, C. Wu, L. Zhang, Z. Jin, ACS Nano (17) (2023) 3209–3224.
[16] S. Ye, Z. Chen, G. Zhang, W. Chen, C. Peng, X. Yang, L. Zheng, Y. Li, X. Ren, H. Cao, D. Xue, J. Qiu, Q. Zhang, J. Liu, Energy Environ. Sci. 15 (2022) 760–770.
[17] W.J. Rogan, M.T. Brady, Pediatrics 123 (2009) e1123–e1137.
[18] G.-F. Chen, Y. Yuan, H. Jiang, S.-Y. Ren, L.-X. Ding, L. Ma, T. Wu, J. Lu, H. Wang, Nat. Energy 5 (2020) 605–613.
[19] W. Zhu, F. Yao, Q. Wu, Q. Jiang, J. Wang, Z. Wang, H. Liang, Energy Environ. Sci. 16 (2023) 2483–2493.
[20] J. Liang, Z. Li, L. Zhang, X. He, Y. Luo, D. Zheng, Y. Wang, T. Li, H. Yan, B. Ying, S. Sun, Q. Liu, M.S. Hamdy, B. Tang, X. Sun, Chem 9 (2023) 1768–1827.
[21] M. Wu, F. Dong, Y. Yang, X. Cui, X. Liu, Y. Zhu, D. Li, O. Sasha, S. Sun, G. Zhang, Electrochem. Energy Rev. 7 (2024) 10.
[22] R. Jia, Y. Wang, C. Wang, Y. Ling, Y. Yu, B. Zhang, ACS Catal. 10 (2020) 3533–3540.
[23] P. Li, Z. Jin, Z. Fang, G. Yu, Energy Environ. Sci. 14 (2021) 3522–3531.
[24] Z.-Y. Wu, M. Karamad, X. Yong, Q. Huang, D.A. Cullen, D.P. Zhu, C. Xia, Q. Xiao, M. Shakouri, F.-Y. Chen, J.Y. Kim, Y. Xia, K. Heck, Y. Hu, M.S. Wong, M.Q. Li, I. Gates, S. Siahrostami, H. Wang, Nat. Commun. 12 (2021) 2870.
[25] M. Jiang, M. Zhu, J. Ding, H. Wang, Q. Yu, X. Chen, Y. He, M. Wang, X. Luo, C. Wu, L. Zhang, X. Yao, H. Wang, X. Li, X. Liao, Z. Jiang, Z. Jin, J. Hazard. Mater. 476 (2024) 134909.
[26] Y. Liu, J. Wei, Z. Yang, L. Zheng, J. Zhao, Z. Song, Y. Zhou, J. Cheng, J. Meng, Z. Geng, J. Zeng, Nat. Commun. 15 (2024) 3619.
[27] W. Zheng, L. Zhu, Z. Yan, Z. Lin, Z. Lei, Y. Zhang, H. Xu, Z. Dang, C. Wei, C. Feng, Environ. Sci. Technol. 55 (2021) 13231–13243.
[28] A. Iarchuk, A. Dutta, P. Broekmann, J. Hazard. Mater. 439 (2022) 129504.
[29] Z. Xi, J. Wang, B. Liu, X. Xu, P. Jing, R. Gao, J. Zhang, J. Energy Chem. 83 (2023) 32–42.
[30] F. Chen, X. Zhou, H. Wang, X. Liu, Q. Yang, X. Chen, Q. Mu, J. Liu, X. Li, X. Liao, Z. Jiang, Z. Jin, M. Jiang, Adv. Funct. Mater. 35 (2025) 2421405.
[31] R. Daiyan, T. Tran-Phu, P. Kumar, K. Iputera, Z. Tong, J. Leverett, M.H.A. Khan, A. Asghar Esmailpour, A. Jalili, M. Lim, A. Tricoli, R.-S. Liu, X. Lu, E. Lovell, R. Amal, Energy Environ. Sci. 14 (2021) 3588–3598.
[32] X. Zhao, Q. Geng, F. Dong, K. Zhao, S. Chen, H. Yu, X. Quan, Chem. Eng. J. 466 (2023) 2.
[33] K. Wu, C. Sun, Z. Wang, Q. Song, X. Bai, X. Yu, Q. Li, Z. Wang, H. Zhang, J. Zhang, X. Tong, Y. Liang, A. Khosla, Z. Zhao, ACS Mater. Lett. 4 (2022) 650–656.
[34] Y. Liu, W. Qiu, P. Wang, R. Li, K. Liu, K.M. Omer, Z. Jin, P. Li, Appl. Catal. B-Environ. 340 (2024) 123228.
[35] L. Bai, F. Franco, J. Timoshenko, C. Rettenmaier, F. Scholten, H.S. Jeon, A. Yoon, M. Rüscher, A. Herzog, F.T. Haase, S. Kühl, S.W. Chee, A. Bergmann, R.C. Beatriz, J. Am. Chem. Soc. 146 (2024) 9665–9678.
[36] J. Yang, H. Qi, A. Li, X. Liu, X. Yang, S. Zhang, Q. Zhao, Q. Jiang, Y. Su, L. Zhang, J. Li, Z. Tian, W. Liu, A. Wang, T. Zhang, J. Am. Chem. Soc. 144 (2022) 12062–12071.
[37] S. Ren, R.-T. Gao, N.T. Nguyen, L. Wang, Angew. Chem. Int. Ed. 63 (2024) e202317414.
[38] S. Ren, R.-T. Gao, J. Yu, Y. Yang, X. Liu, L.W.L. Wang, Angew. Chem. Int. Ed. 63 (2024) e202409693.
[39] M. Jiang, A. Tao, Y. Hu, L. Wang, K. Zhang, X. Song, W. Yan, Z. Tie, Z. Jin, ACS Appl. Mater. Interfaces 14 (2022) 17470–17478.
[40] Y. Wang, H. Li, W. Zhou, X. Zhang, B. Zhang, Y. Yu, Angew. Chem. Int. Ed. 61 (2022) e202202604.
[41] M. Jiang, J. Su, X. Song, P. Zhang, M. Zhu, L. Qin, Z. Tie, J.-L. Zuo, Z. Jin, Nano Lett. 22 (2022) 2529–2537.
[42] Y. Han, X. Zhang, W. Cai, H. Zhao, Y. Zhang, Y. Sun, Z. Hu, S. Li, J. Lai, L. Wang, J. Colloid Interface Sci. 600 (2021) 620–628.
[43] W. Zhang, Z. Jin, Z. Chen, Adv. Sci. 9 (2022) 2105204.
[44] X. Liu, X. Cai, Y. Zhu, Acc. Chem. Res. 56 (2023) 1528–1538.
[45] M. Yao, M. Zhu, Z. Yang, X. Song, X. Yuan, Z. Zhang, W. Hu, J. Xie, Nat. Rev. Mater. 10 (2025) 89–108.
[46] Y. Xiong, X. Liu, Y. Hu, D. Gu, M. Jiang, Z. Tie, Z. Jin, Nano Res. 15 (2022) 4965–4972.
[47] J.L. Zeng, Z.-J. Guan, Y. Du, Y.-M. Lin, Q.-M. Wang, J. Am. Chem. Soc. 138 (2016) 7848–7851.
[48] Z. Lei, X.-L. Pei, Z.-J. Guan, Q.-M. Wang, Angew. Chem. Int. Ed. 56 (2017) 7117–7120.

[49] Z. Shen, Y. Yu, Z. Zhao, S. Zhang, S. Xu, S. Yang, Y. Hu, J. Hazard. Mater. 445 (2023) 130651.
[50] Y.X. Duan, F.L. Meng, K.H. Liu, S.S. Yi, S.J. Li, J.M. Yan, Q. Jiang, Adv. Mater. 30 (2018) 1706194.
[51] H. Wang, Z. Zhang, H. Yin, Y. Wu, Appl. Catal. A-Gen 614 (2021) 118055.
[52] Y. Cudennec, A. Riou, Y. Gérault, A. Lecerf, J. Solid State Chem. 151 (2000) 308–312.
[53] L. Su, K. Li, H. Zhang, M. Fan, D. Ying, T. Sun, Y. Wang, J. Jia, Water Res. 120 (2017) 1–11.
[54] F.-Y. Chen, Z.Y. Wu, S. Gupta, D.J. Rivera, S.V. Lambeets, S. Pecaut, J.Y.T. Kim, P. Zhu, Y.Z. Finfrock, D.M. Meira, G. King, G. Gao, W. Xu, D.A. Cullen, H. Zhou, Y. Han, D.E. Perea, C.L. Muhich, H. Wang, Nat. Nanotechnol. 17 (2022) 759–767.
[55] X. Ouyang, W. Qiao, Y. Yang, B. Xi, Y. Yu, Y. Wu, J. Fang, P. Li, S. Xiong, Angew. Chem. Int. Ed. 64 (2025) e202422585.